Chapter 3. Incubation

3.1 Topological investigations

Topological investigations of the surface can provide a first level of information on the ablation process. The visual inspection gives valuable indications of the mechanisms, as discussed below. This chapter presents an overview of different ex-situ techniques for analyzing the irradiated surface. It will be shown that a suitable choice of laser parameters can tune the transition between different processes, balancing between non-thermal and thermal mechanisms. The most dramatic effect comes from employing ablation regimes with different number of shots per site (N). It will be shown below that N, the number of pulses per site, and to a lesser extent the laser fluence (F) and pulse duration (τ_L), govern the transition between different ablation phases and subsequently mechanisms.

Sapphire is a particularly interesting candidate for a detailed study of the ablation mechanisms since it clearly exhibits two completely different ablation phases, a gentle, smooth sputtering followed by a strongly violent explosive ablation phase [TBC89, ARV97]. The two-phase behavior has not been observed for the more conventional, ns, laser induced processing [TBC89]. For ultrashort irradiation, different etch phases have been identified for other dielectric materials as well [SAR2000], e.g. fused silica or crystalline quartz as will be discussed later in this chapter. The strong differences between these reported phases are reviewed below. One of the main arguments underlining the existence of different ablation processes is based on scanning electron microscope (SEM) pictures of the irradiated area for different pulse durations and number of pulses per site. This is illustrated in Fig. 3.1-1 and Fig. 3.1-2. The first laser shots above the damage threshold (at 4 J/cm^2) initiate the “gentle etch-phase”. For 200 fs irradiation the gentle etch-phase (N<30 at 4 J/cm^2) is characterized by an extremely smooth surface (sometimes even smoother than the initial state), both at the side-wall and at the bottom of the structure with almost no pattern developing except ripples and with no particulates around the rim (Fig. 3.1-1, Fig. 3.1-2-(a, b)). Material is removed with every laser pulse, including the first pulse. The ablation rate is low, around 20-30 nm/pulse as determined by Atomic Force Microscopy (AFM), as reported in [ARV97]. As will be argued in the next chapters, the mechanism for material removal appears to have an electrostatic origin.

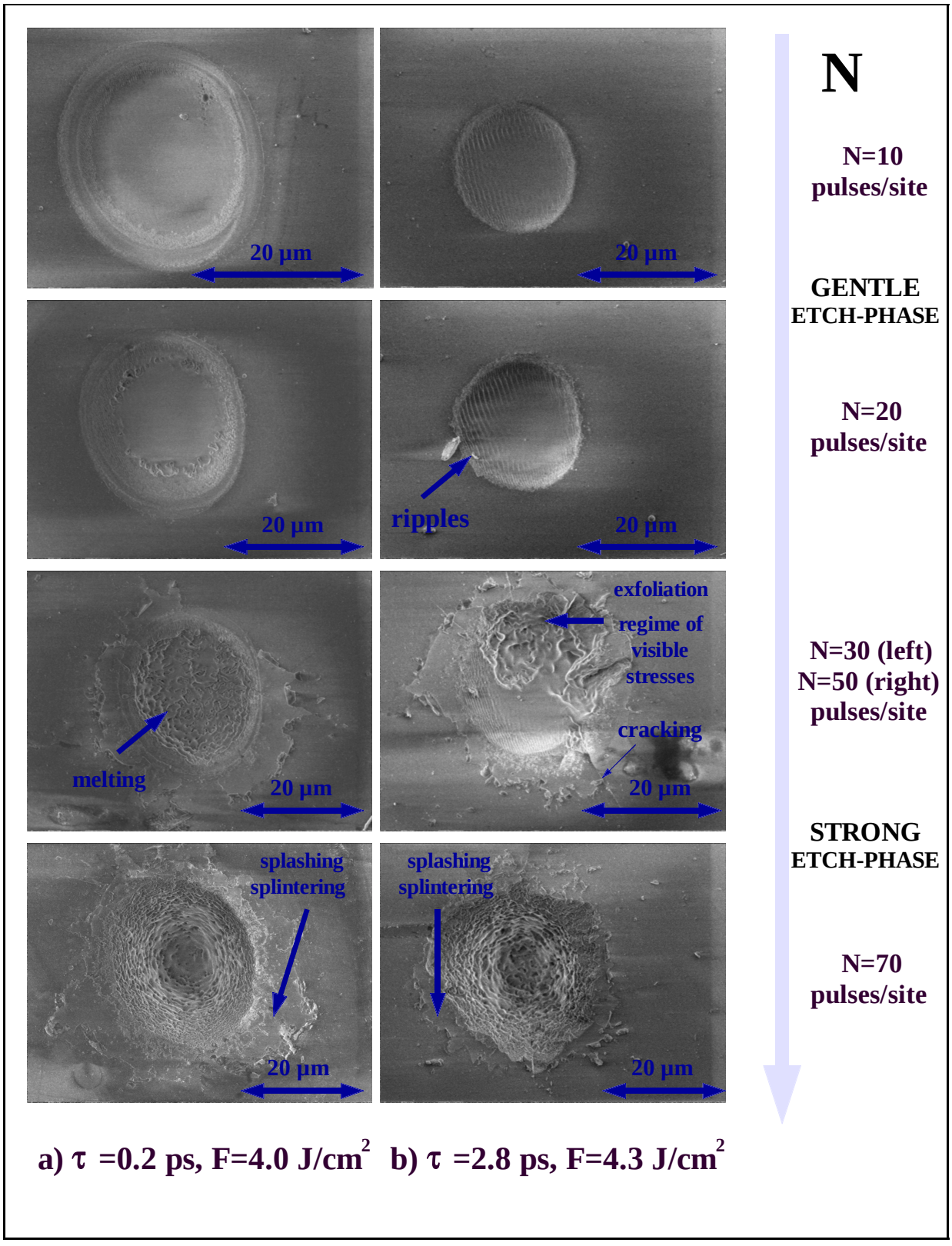

Fig. 3.1-1 Scanning electron microscope (SEM) pictures of a sapphire surface irradiated with 0.2 ps at 4.0 J/cm^2 (a) and 2.8 ps pulses at 4.3 J/cm^2 (b), the wavelength being 800 nm, and the number of pulses per site being: *N*=10, 20, 30/50, 70. One can note the transition from the gentle to the strong etch-phase. The laser was at normal incidence. The quality of the structures is greatly decreased for ps pulses as a consequence of stress accumulation in the Al_2O_3 sample. The stress load is an outcome of the combined result of the enhanced thermal and self-focusing effects.

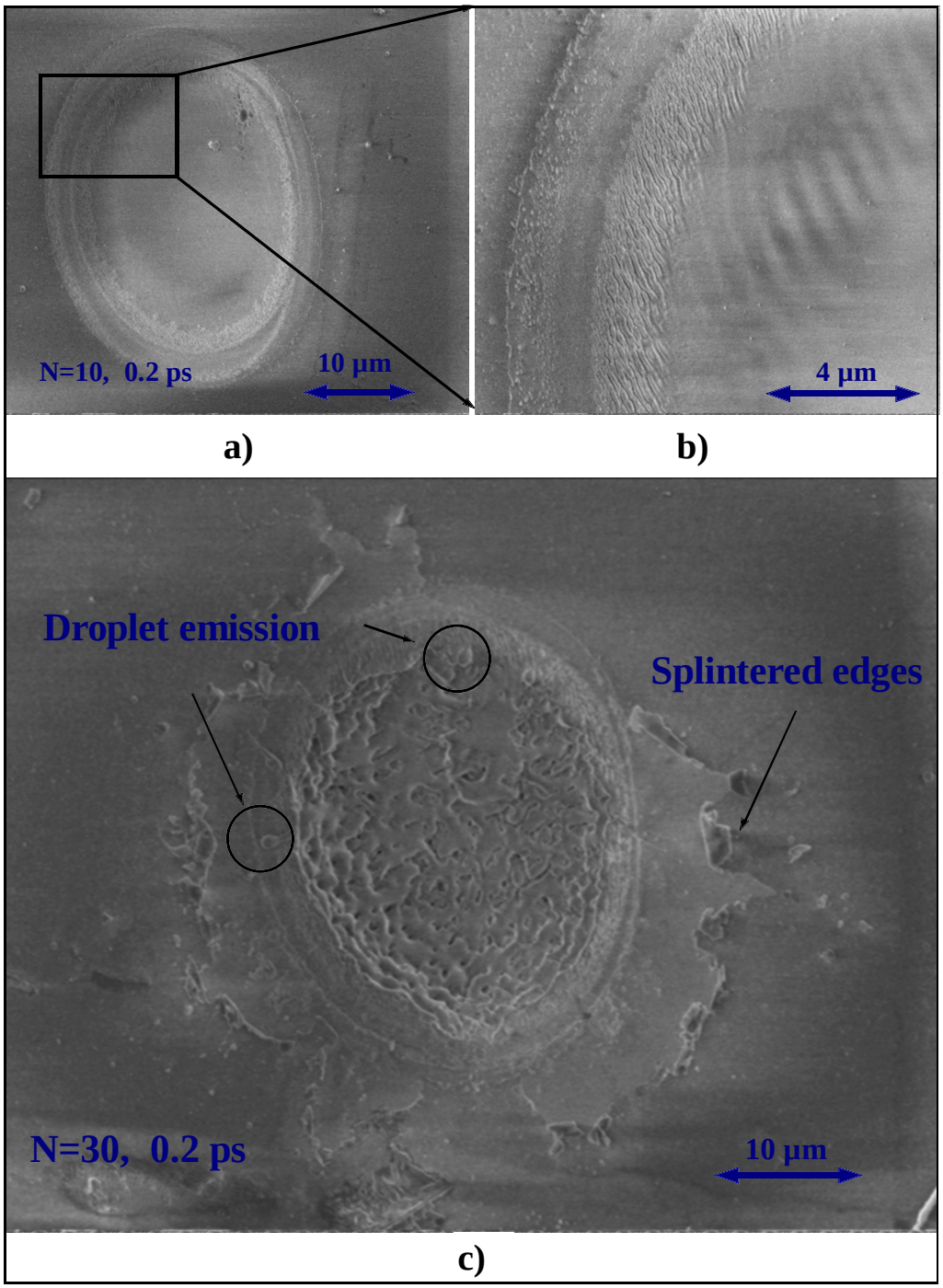

Fig. 3.1-2 SEM pictures of the laser impact spot for sapphire at 0.2 ps pulse duration. a) Irradiation spot for *N*=10; gentle etch-phase (as seen in Fig. 3.1-1, first row, left column). b) Example of ripples in 0.2 ps regime; enlarged detail of a). Note the two different types of structures, dense ripples at the edge with a spacing of about 0.2 µm, and interference ripples with a spacing related to the wavelength (~ 0.8 µm). c) Enlarged view of the irradiation spot for *N*=30 (as seen in Fig. 3.1-1, third row, left column). Droplets and splintered edges are visible.

At a higher number of laser pulses per site, the appearance of the spot changes dramatically and the surface shows the characteristics of the strong ablation phase. That means greatly increased roughness and also an increased quantity of material removed, as will be seen later. Visual inspection reveals characteristics of a violent mechanism of thermal

nature, among them droplets, melting traces, splintered edges. Increasing the number of shots will result in crater formation.

At this particular fluence, slightly above the single shot threshold, the crossover from the gentle to the strong etch-phase takes place between 25 and 30 laser pulses per site for this pulse duration, when the irradiated spot shows a greatly increased roughness (Fig. 3.1-1, Fig. 3.1-2 (c)) of the depression bottom and a much higher ablation rate (~300 nm/pulse). In this violent sputtering regime, intensely luminous material is ejected. Numerous particulates are redeposited around the rims, and the splashed solidified liquid together with the formerly molten material inside the spot and with the splintered aspect of the edges can be taken as evidence for a violent thermal mechanism responsible for particle removal. It will be demonstrated below and in the next chapters, based on the occurrence probability for different thermal channels, that the relevant process is phase explosion, which is basically thermal [KeM96, ZKG97]. After 70 pulses per site a crater with a ~20 µm depth and a ~30 µm width was present. The layered structure of the walls of the crater corresponds to the contribution to the material removal of each pulse in the strong etch-phase. After a certain depth the walls became smoother due to material redeposition (not shown in the figure).

Ripple formation

We have stated that the gentle ablation phase is distinguishable by the smooth surface left after irradiation except for the regular ripple patterns observed.

In the case of sapphire, particularly for irradiation at 2.8 ps, the gentle etch-phase demonstrates a clear ripple pattern, which develops perpendicular to the laser electric field vector (Fig. 3.1-1).

Ordered patterns have been observed also in the 0.2 ps regime (Fig. 3.1-2 (b)), under certain conditions of incubation, however it appears that ps pulses enhance the probability of ripple formation. The ripples are spaced by a distance approximately corresponding to the laser wavelength (~0.7–0.8 µm) and the modulation depth is on a few nm to tens of nm range, depending on the pulse duration [ARV97, VWR98, Bau96]. The formation of ripples is mainly characteristic for the gentle etch-phase and continues briefly into the strong etch-phase, until the violence of the material removal destroys any ordered pattern. The mechanism of ripple formation is presumably related to the modulation of the free-electron density (and the related dielectric response) during the interference between the incoming and surface-scattered laser light [ARV97, AHR98] (which results in a pattern of standing waves) since the spacing correlates with the laser wavelength and the pulse duration is too short for thermal effects to be fully developed during the pulse duration (this holds especially in the case of

femtosecond irradiation, for picosecond pulses certain heating is expected during the pulse but without significant removal occurring within this interval). The scaling with λ rather than λ/n suggests a change from the dielectric to a metallic behavior due to the rapid build-up of electrons in the conduction band. No stoichiometric changes, and, hence, no metallization of the surface have been observed.

A second type of ripple has been observed at the edges of the irradiation spot, in the gentle etch-phase regime, with a spacing of ~0.2 μm (Fig. 3.1-2 (b)). This kind of pattern has been previously associated with laser-induced surface-stress relaxation [KrK96].

It is still unclear to what extent thermal effects contribute to ripple formation on dielectrics. However, with ultrashort laser pulses, the material-dependent lifetime of the electrons in the conduction band appears to play an important role in the probability of ripple formation [AHR98]. Fig. 3.1-3 shows, for example, that in the case of fused silica, ripples seen for 0.2 ps pulse durations have a much higher contrast that the ordered patterns produced for picosecond irradiation. Fused silica has a much shorter lifetime of the electrons in the conduction band (these being trapped as self-trapped excitons in about 150 fs [DGK94]) in contrast to sapphire, where the electrons can survive inside or just in shallow traps under the conduction band for almost 100 ps. At low fluences (4.2 J/cm^2) the ripples are oriented parallel to the polarization vector, being spaced by approx. 0.67 μm, and they develop further in the strong phase, while ripples perpendicular to the polarization vector have been seen at higher fluences (12.5 J/cm^2) mainly in the gentle phase, and their spacing is closer to the laser wavelength (~0.74 μm). Fig. 3.1-4 illustrates the laser polarization effect on ripple orientation for both sapphire and fused silica samples.

Ripple formation has been observed also for nanosecond irradiation (especially for metals and semiconductors) but their nature seems to be of thermal origin related to the instabilities induced in the molten layer [RoK84, KeR85, Bau96]. An interpretation has been given based on defect initiating field enhancement or interference field patterns with subsequent induced polarization and hence a modulated energy transfer to the lattice [PAB91, TeS81] in a quasi-stationary fashion. Short laser pulse (1 ps) investigations [AAF99] on absorptive/conductive materials (graphite) where lattice heating and phase transformation take place after the pulse end, being totally decoupled from the primary absorption mechanisms, demonstrated that ripple formation in that case is initially associated with the excitation of the surface electromagnetic waves accompanied by the diffraction of the incident laser wave and the formation of a temperature grating.

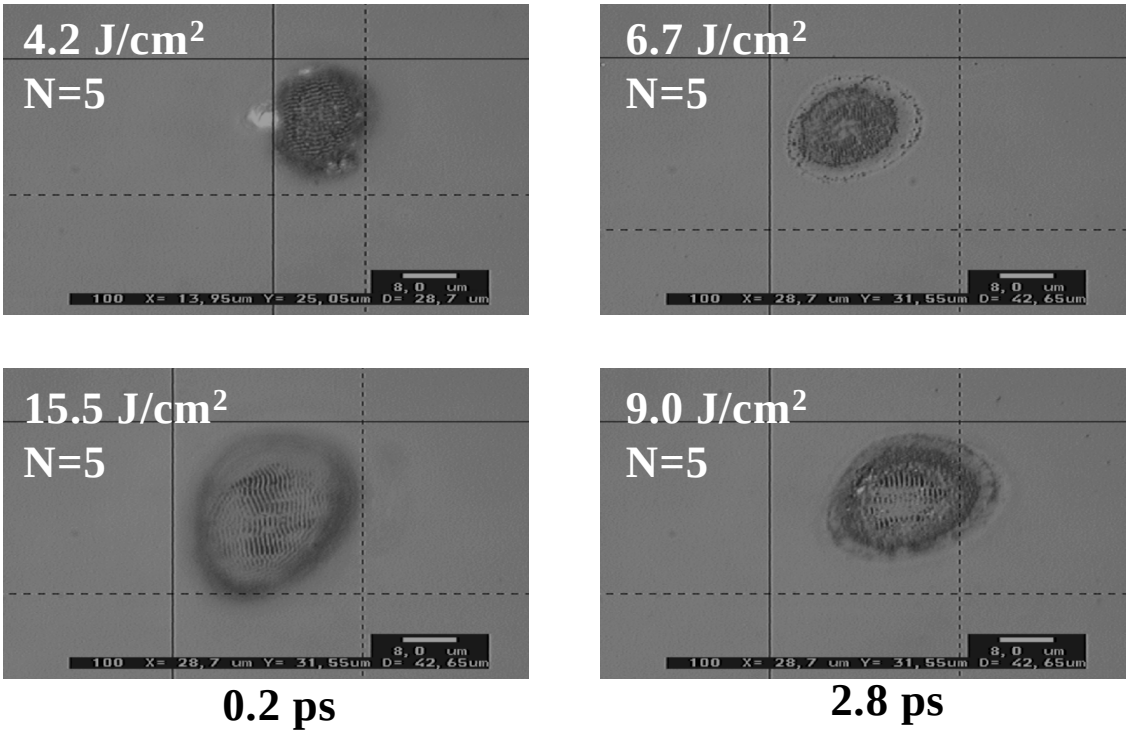

Fig. 3.1-3 Ripple formation on laser irradiated fused silica samples at different fluences and pulse durations.

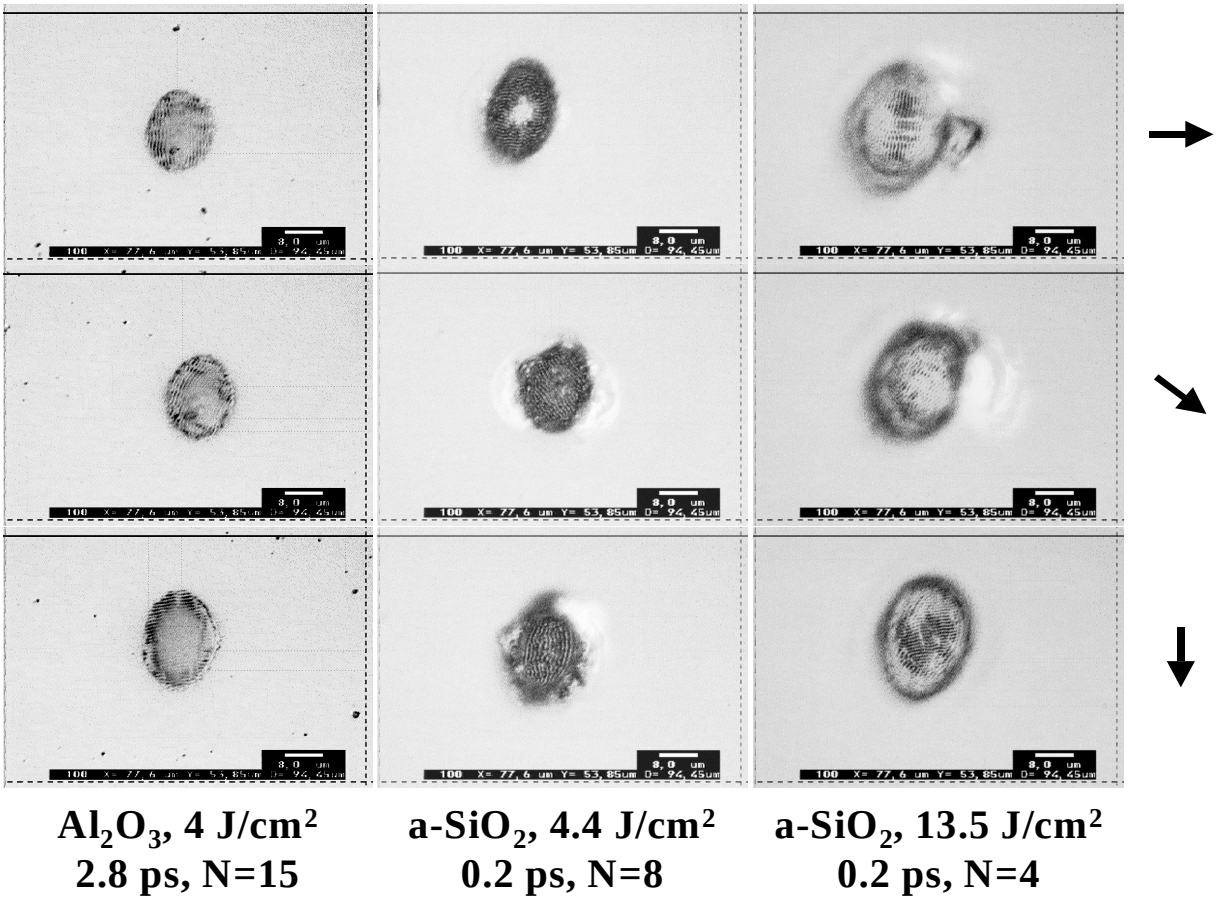

Fig. 3.1-4 Ripple orientation is polarization dependent. The arrows on the right side show the orientation of the laser electric vector.

Subsurface heating

Another type of information can be extracted from Fig. 3.1-1. Strong differences in the strong sputtering regimes of ablation are seen as a function of the pulse duration. As can be noticed in the right column of Fig. 3.1-1, in the case of picosecond irradiation the strong etch-phase is a regime of visible stress displaying exfoliation and cracking at the edges (in contrast to the 0.2 ps regime, where the irradiated spot shows firm rims and cracking is not observed for the number of pulses employed in the experiment).

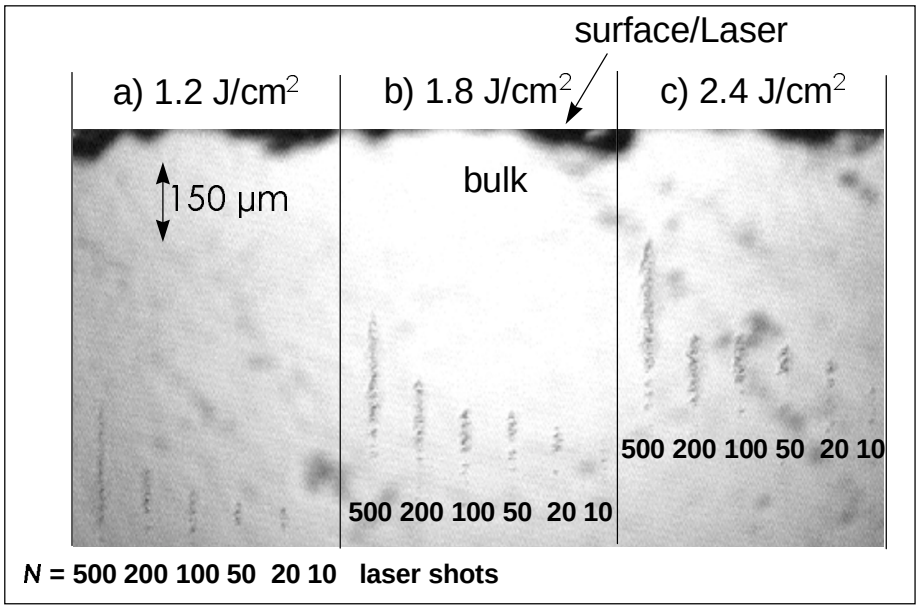

Fig. 3.1-5 Sub-surface/bulk modifications as a consequence of laser self-focusing at 2.8 ps. Incubation as a result of multiple irradiation or increased energy will determine the damage extension towards the surface

As was previously reported for ps pulses [AHR98], besides enhanced thermal effects we observe damage beginning *beneath* the surface, i.e. sub-surface damage, caused by beam narrowing (self-focusing) of ps pulses inside the sapphire sample, which leads to a maximum density of excitation underneath the surface. This can be seen in Fig. 3.1-5. Increasing the number of laser pulses at the same point of impact causes the damage to grow towards the surface [AVR98] and under certain conditions it may even reach the interface. This eventually can lead to cracking, exfoliation, thermal and mechanical stress, and, finally, adds to the explosive thermal ejection mechanism as indicated by the splashed material around the rims of the crater. (Fig. 3.1-1, Fig. 3.1-2 (c)). Exfoliation and splintered material have also often been associated with thermal shock which is incompletely relaxed by melting, especially for materials with a high linear thermal expansion coefficient, high melting point, and high Young's modulus. Sapphire is a material that possesses these properties, so repeated thermal shocks, unrelieved by extensive melting at the edges of the spot due to the Gaussian spatial

profile of the laser, would finally lead to cracking, splintering, and exfoliation [KCL85]. But it should be noted that, in addition to the above mentioned mechanisms, in the ps regime, where self-focusing plays a major role, exfoliation and cracking may be due to shock release from beneath the surface. This appears to be one of the very few real examples that provides evidence for the existence of what could be characterized as sub-surface heating (note that the laser pulse was primarily focused on the surface).

Gentle to strong transition

After this overview of the experimental data characterizing the ablation phases we can have a closer look at a possible explanation for the observed facts.

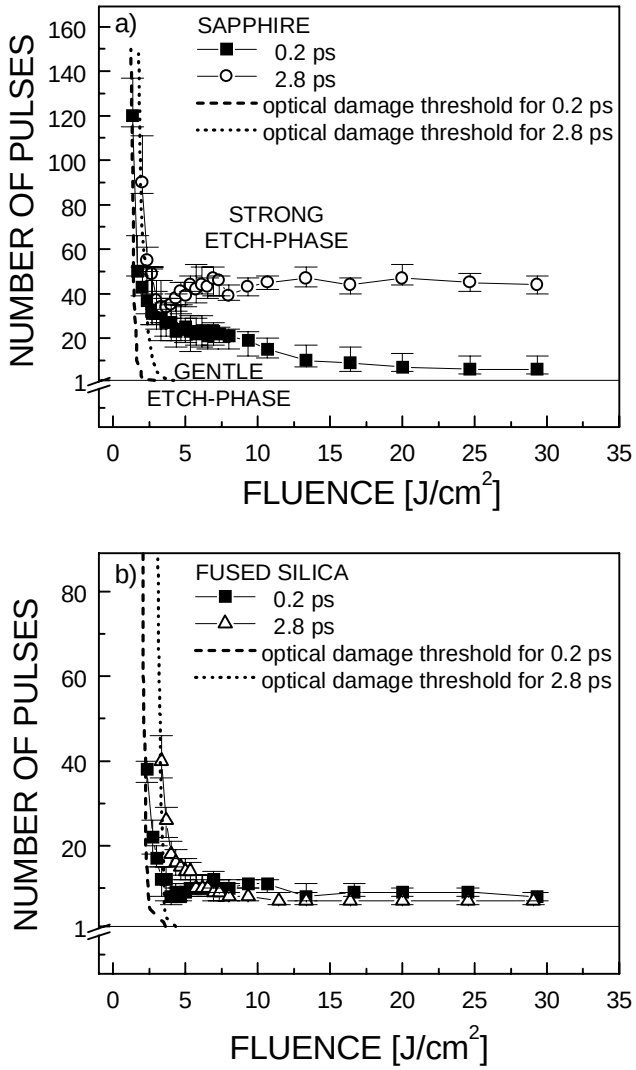

Fig. 3.1-6 Gentle to strong crossover *N*-values for different fluences and two different pulse durations: 0.2 ps and 2.8 ps in the case of sapphire and fused silica samples. For high energy/shorter pulses the gentle to strong crossover takes place for lower *N*.

It was suggested earlier that an incubation phenomenon plays a dominant role for the formation of a strong phase. We have studied this transition for different fluences and the

observations are illustrated in Fig. 3.1-6 and summarized below. Fig. 3.1-6 depicts the gentle to strong crossover values as determined by visual inspection of ablation for different laser parameters. The values depicted in Fig. 3.1-6 are measured when the area affected by the strong etch phase is 2/3 of the whole spot surface.

The crossover from the gentle to the strong etch-phase (Fig. 3.1-6) represents the transition to a violent regime of predominantly thermal nature and is governed by the ability of the irradiated system to transfer heat to the lattice in an efficient way. For the fluences employed in this experiment this is determined by the rate of incubation. At high fluences, when the crossover occurs after a low number of pulses, incubation plays a less dominant role and the energy is mainly thermally deposited into the lattice by enhanced electron-phonon coupling without major assistance from laser induced defects acting as trapping sites. It also appears that the gentle to strong transition is more efficient for shorter pulse durations. This can be motivated by the fact that the incubation rate is strongly pulse duration dependent, taking place for lower number of shots per site for femtosecond pulse as compared to picosecond pulses (pumping from defect states is more efficient for high intensities). Also, during the picosecond pulse, enhanced thermal effects can lead to the annealing of defects.

When the number of pulses per site is increased for both pulse durations, one finds that, due to defect formation and incubation effects, spatially localized absorption centers (often color centers) as well as permanently induced defects (morphological and structural changes) are formed [JBC89, EGG98, ALS99]. They are distributed in accordance with the laser pulse spatial profile, with a maximum formation probability at the center of the profile [JBC89]. The result is an increased absorption coefficient, a direct absorption from the surface-defect states, and a greatly enlarged amount of energy deposited. This increases the probability of having different channels to transfer energy to the lattice, decreases the selectivity of recombination (defects act as trapping sites and contribute to a more efficient energy redistribution from the electrons to the lattice besides the electron-phonon coupling), and leads to an ablation mechanism which resembles thermal violent mechanisms for particle removal. These mechanisms in general involve splintered edges, as well as splashed liquid and molten droplets around the rims of the irradiated spots [KCL85, MiK95, BaF73, RoK84].

A very important observation is that the ablation rates are much higher in the strong phase. We can observe a steep increase from less than 30 nm per pulse in the gentle phase to more than 300 nm per pulse in the strong ablation phase (Fig. 3.1-7, (a, b)). If in the case of the gentle phase the efficient absorption is restricted to the electron plasma, for the strong phase the absorption zone will be enlarged due to the presence of defects. This, together with

enhanced thermal transport explains the higher ablation rates observed in the strong ablation phase.

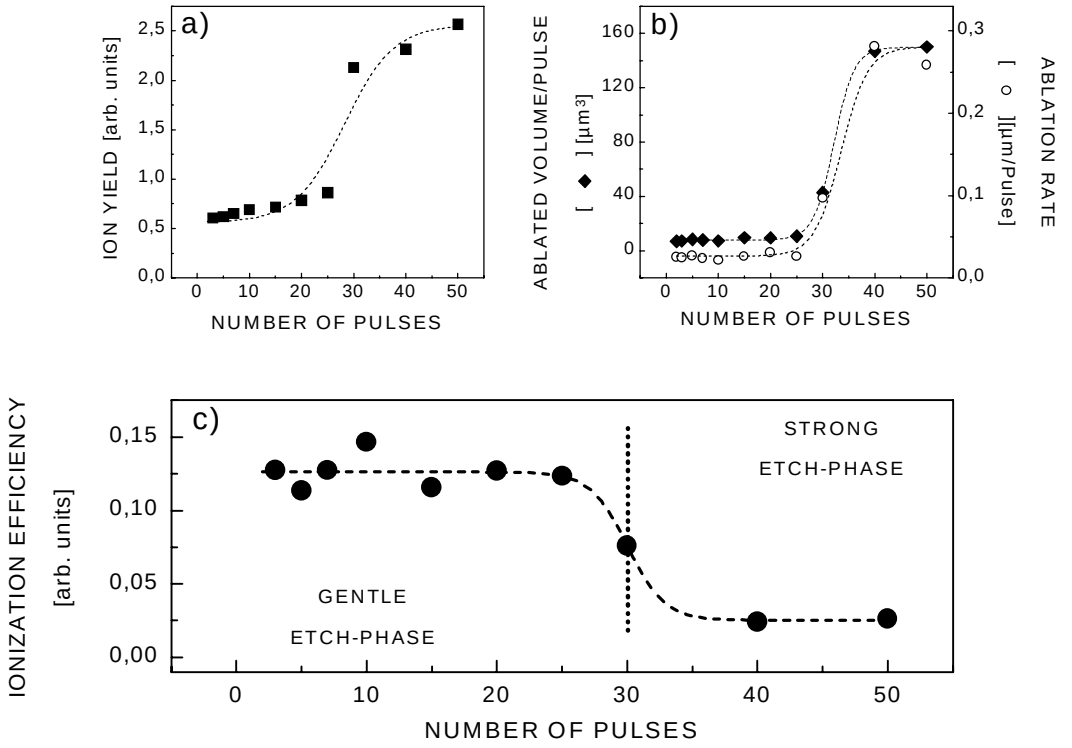

Fig. 3.1-7 The relative ion yield (a), the ablation rate and the volume of the ablated material (b), and ionization efficiency (the ratio between the number of ions and the total amount of particles being ablated) versus the number of pulses at 4 J/cm^2 and 0.2 ps pulse duration (c). The gentle etch-phase shows higher ionization efficiency than the strong etch-phase.

The different nature of the two mentioned ablation phases is underlined by determining the relative number of ions emitted with respect to the total amount of particles ablated per pulse[1]. These measurements have been done by estimating the total number of ions (integrated over velocity and angular distributions, and making some reasonable assumptions concerning the detection efficiency) and the total number of particles emitted considering the volume of the material being ablated. The ionization degree is given by the ratio of these two quantities.

While both the total ion yield and the ablation rate increase with the number of shots with a steep augmentation at the crossover, the two observed phases have clearly different ionization efficiencies. The gentle etch-phase is a process with high efficiency in ion production (~10%), which decreases at the crossover to the strong etch-phase. This can be

[1] See Appendix 2

clearly seen in Fig. 3.1-7-(c). This observation will be discussed in detail in the next chapter in connection with the velocity distributions of the removed particles.

At the same time the amount of material determines the properties of the plume and initiates the formation of a high-density plasma.

The plume luminosity also correlates with the two ablation phases observed ex-situ. This is illustrated in Fig. 3.1-8.

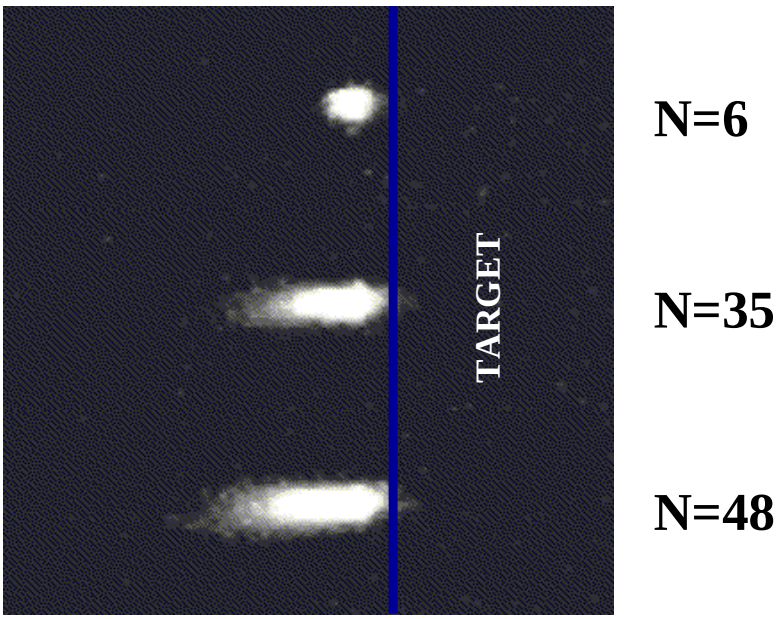

Fig. 3.1-8 Plume emission pictures under the conditions corresponding to the gentle (N=6) and strong ablation phases (N=35, 48) respectively.

Here the light scattering or emission is detected by a CCD camera. For low numbers of laser shots, i.e. when the ablation is still in the gentle phase, only a small amount of light scattered from the substrate surface is detected. As soon as the crossover to the strong ablation phase occurs (for N>30) (as characterized by an increase in the amount of material removed per pulse and the appearance of low velocity ions), a strong light emission is detected from the plasma plume.

3.2 Incubation

During and shortly after the laser pulse, non-linear photon-induced excitation processes, i.e. multiphoton seeded avalanche ionization will give rise to the development of an electron-hole plasma. Recombination of the electron-hole pairs will eventually eliminate the plasma, however, a few pairs may escape annihilation. For example some of the electrons may be captured by structural defects or impurities. There is also a finite probability that electron-hole

pairs will separate to develop stable defects with energy states inside the band gap. Single, low-order or resonantly enhanced high-order multi-photon excitation from these new defects states generated by earlier laser pulses will give an additional contribution to the plasma concentration during the next laser pulse. This may eventually cause the laser-induced electron-hole plasma to reach a critical concentration leading to damage at lower laser energies.

Minor alterations in the energy structure of the wide band gap materials may have a major impact in the absorption cross section for highly non-linear excitation. Cumulative effects (stress load associated with volume expansion due to defects [JBC89]) will accentuate this.

Sapphire Al_2O_3

Although there is a low probability to form color centers in sapphire as a direct effect of the electronic excitation/ionization, defects can be induced by strong ionization related atomic displacements. Generally, induced excitons have a lifetime of about 100 fs, self-trapped excitons have a relaxation time of 1 ns (above room temperature), while the vacancy-interstitial pairs relax on a very long time scale. At the sample surface it is much easier to generate vacancy-interstitial pairs or just vacancies following the preferential emission of a certain chemical species than it is in the bulk where the probability for recombination is much higher [Ito99].

After the thermalization of the laser induced electron-hole plasma in sapphire, some of the electrons may be captured by structural defects or impurities, and, thus, excluded from their further recombination with holes. As a result, the concentration of thermalized holes *h* in the affected zone will be higher than the concentration of thermalized electrons, which leads to a predominant formation of F^+ centers based on single electrons trapped on oxygen vacancies. As shown by luminescence studies from Al_2O_3 irradiated with heavy ions, the F^+ formation occurs via the reaction [Sku98]:

$$F^0 + h^+ \rightarrow \left(F^+\right)^* \rightarrow F^+ + h\nu\left(3.8eV\right)$$

Here, the $(F^+)^*$ is the excited state of a F^+ center. Simultaneously with this process the ionization of the F^+ also takes place via the channel:

$$F^+ + h^{+-} \rightarrow \left(F^{++}\right)^* \rightarrow F^{++}$$

with a non-radiative relaxation of the F^{++}-center excited state (“empty” anion vacancy). The next capture of an electron at the F^{++}-center is also accompanied by the F^+ center excited state formation:

$$F^{++} + e \rightarrow \left(F^{+}\right)^{*} \rightarrow F^{+} + h\nu\left(3.8eV\right)$$

Also evidence for *F* centers (oxygen vacancies with two trapped electrons) has been obtained in electron irradiated sapphire from observing luminescence at 300 nm [CaC93], or 315 and 413 nm, [AMY96], besides the F^{+} centers emitting at 325 nm.

The defect level representation in sapphire is presented in Fig. 3.2-1.

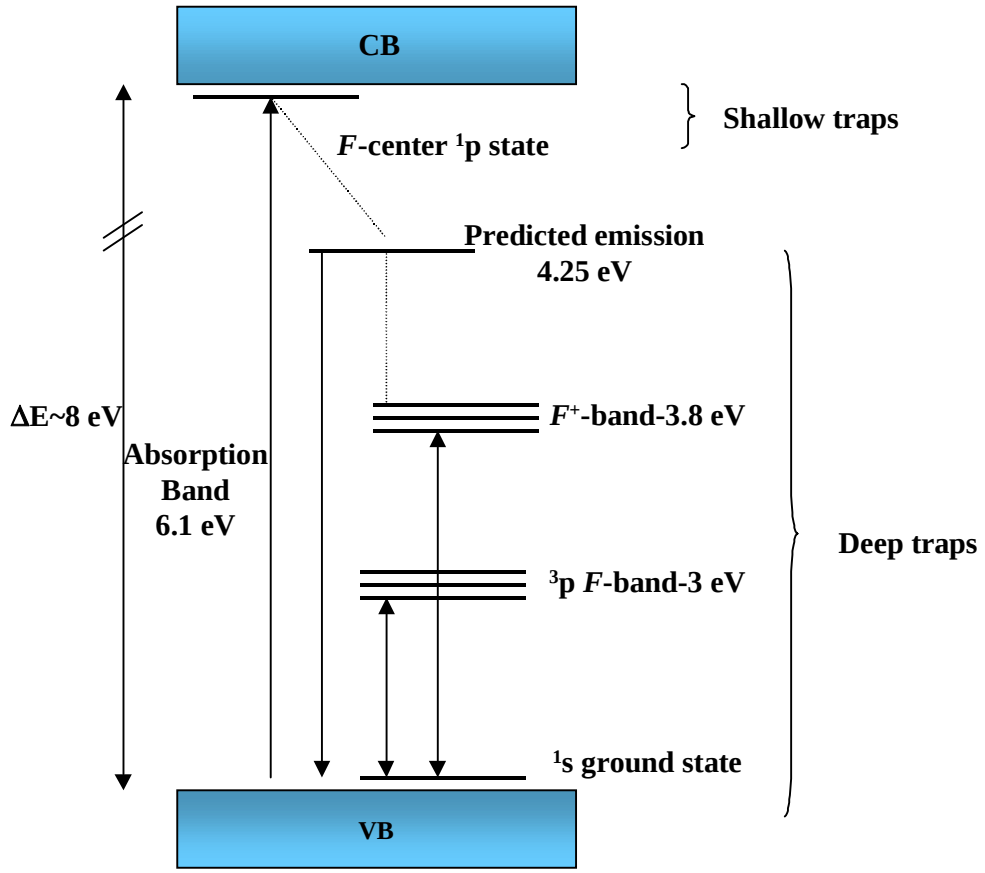

Fig. 3.2-1 Defect levels in sapphire (adapted from [CaC93]).

The general picture for sapphire consists of two types of electron trapping sites: shallow (low-energy) electron traps and deep (high-energy) electrons traps, with a single hole trap which acts as a recombination center, the charge carrier trapping being important in radiation induced breakdown. The shallow traps empty at room temperature, detrapping time being exponentially dependent on the trap depth. The trapping sites lie within less than 0.5 eV below the conduction band [CaC93]. The "free" electron characteristic time for sapphire before trapping in the high energy traps is about 100 ps [QGM99].

Fused silica SiO_2

From luminescence studies the defects in fused silica have been identified as E_1' centers. The experimental data by Saeta et al. [SaG93] suggest that the primary photophysical

event following laser absorption in fused silica is the creation of a “bound” electron-hole pair (singlet exciton) that decays into a non-relaxed Frenkel pair (nonbridging oxygen hole center NBOHC [≡Si-O•]-E’ center [≡Si•]) state in 0.25 ps as has been determined from optical transient spectroscopy (“–,•” denotes bond and lone pair electron). This type of primary defect pair proved to be the self-trapped exciton (STE) [SaG93, PDG96] following a fast initial lattice relaxation. Fast and efficient trapping of the conduction band electrons into the STE’s states has been also observed on the 150 fs time scale by Petite et al. [PDG96] in a phase retardation interferometric setup based on measurements of the free electron population density in fused silica.

The defect level and structure in fused silica is presented Fig. 3.2-2.

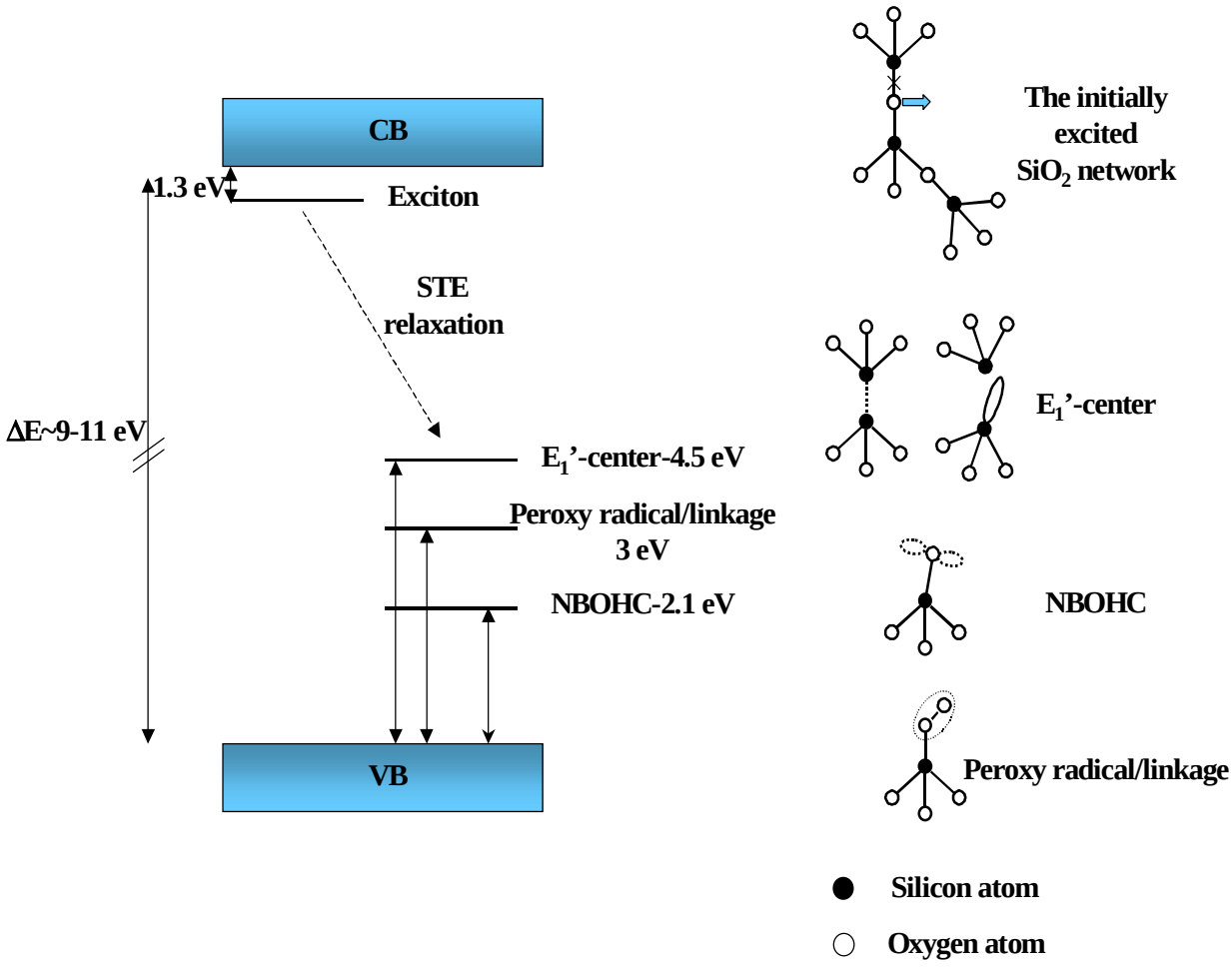

Fig. 3.2-2 Defect levels and structure in fused silica (adapted from [DeF86]).

The general consensus in the case of fused silica is that the band-gap value is approximately 9-11 eV, with a Wannier exciton state lying ~1.3 eV below the conduction band minimum. The type and size of the singlet exciton can be estimated from the character of the band edge states. Those at the top of the valence band are most likely nonbonding oxygen *p* states, and are characterized by a large hole effective mass m_h~*(5-10)*m_e. Those of

the conduction bands are primarily silicon s states, although they appear to have a finite admixture of silicon-oxygen antibonding character, and have an effective mass of *~(0.3-0.5)*m_e. The exciton radius is 0.28 nm, larger than the Si-O separation of 0.16 nm. Because of its large mass, the hole of the exciton is localized on the oxygen atom, while the electron is appreciably delocalized over the nearby silicon atoms [SaG93]. Consistent with the finite antibonding character of the electron state, it is envisioned that electronic excitation reduces the Si-O bond strength and facilitates exciton self-trapping, i.e., the electron and hole become a localized Frenkel pair (with absorption at 5.2 eV). Theoretical studies (see [SaG93] and the references therein) have shown that the singlet exciton decays either by relaxing to its ground state or into the lower energy configuration of a triplet state. When the oxygen atom on which the hole is located moves away from one of the silicon atoms to which it was bonded, the associated electron becomes localized on that silicon atom and undergoes a spin flip. The triplet exciton in its equilibrium configuration has the optical characteristics of the E' center (an oxygen vacancy with a trapped hole on one of the adjacent silicon atoms, leaving an impaired electron in a dangling sp^3 hybrid orbital of the other adjacent silicon, bound to the remaining three O atoms). The formation of E' centers is favored by the preexisting O vacancies and the ionization of the corespondent Si-Si bond [SoW96, DeF86, LPH91]. The O atom that has moved from the equilibrium position in the SiO_2 tetrahedra, after the respective bond to one of the adjacent Si atoms has been weakened, goes into the NBOHC state and may end up in a peroxy linkage [≡Si-O-O-Si≡] or radical [≡Si-O-O•] after covalently coupling to another O atom, either part of the tetrahedra or interstitial.

We have seen that incubation (the defect accumulation process) is responsible for the above reported transition from the gentle-etch phase to the strong ablation regime. The incubation effects will also have a strong influence on the ablation thresholds for multiple irradiation.

Definition of the ablation threshold

The ablation threshold is characterized by a burst of emitted particles, ions and neutrals. Although the optical damage threshold has been defined as the smallest observable modification in a Nomarski microscope, it can be derived more precisely from the extrapolation of the damage dimension represented as a function of the laser fluence at different numbers of shots per site, to the zero value. Assuming a Gaussian spatial laser profile, the area of the damage will follow an exponential behavior with the laser fluence. On a semi-logarithmic plot, its intersection with the zero level gives the respective threshold. The extrapolation process is illustrated in Fig. 3.2-3 for both the gentle and the strong phases. On

this graph, the damage dimension follows a linear dependence on the fluence logarithm in the gentle phase, until the strong phase takes over, dominating the irradiated surface.

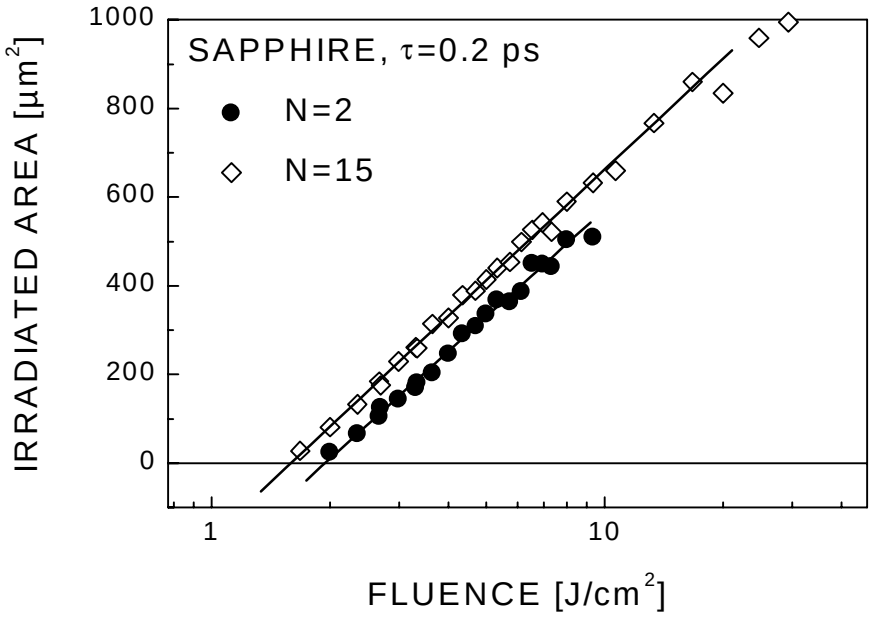

Fig. 3.2-3 Extrapolation lines for threshold determination. The optical damage dimensions are measured for the sapphire sample at 200 fs irradiation at different number of shots per site as a function of the laser fluence (see text for details).

Just above the threshold, when a clear mark is observed within the laser spot whenever the local energy density has exceeded the local threshold, the boundaries of the affected region satisfy the threshold condition As in Eg E 2.3-1, 2.3-2, we can write:

$$F(r) = F \exp\left(2 \frac{S_{damage}}{S_{spot}} \right) \qquad \text{E 3.2-1}$$

where $S_{damage}=\pi r^2_{damage}$ represents the area where the fluence was exceeding the material threshold:

Thus the threshold fluence can be determined by the condition:

$$S_{damage} = \frac{S_{spot}}{2} [\ln(F) - \ln(F_{th})] \approx 0 \qquad \text{E 3.2-2}$$

The incubation strength can be estimated from Eq. E 1.3-13, based on the assumption that multiphoton produced electrons from both valence band or defect states are seeding the avalanche process for each laser shot. The main assumption is that the damage occurs at the critical electron density independent of the particular channels for energy deposition in different materials. It was shown in Chapter 1 that this assumption holds better for short

pulses, below a few hundred femtoseconds or for materials with a long lifetime (>ps) for the free electrons (e.g. sapphire).

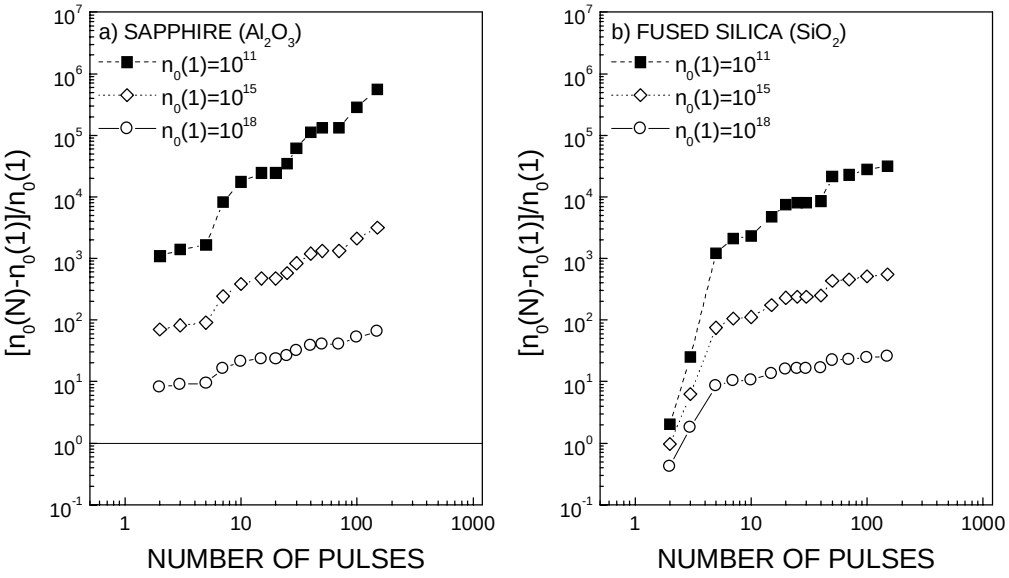

Fig. 3.2-4 Threshold defect accumulation process, based on the optical damage threshold model developed by Stuart et al. [SFH96] for 0.2 ps irradiation of sapphire and fused silica. The curves are calculated from Eq E-1.3-13 and Eq. E 3.2-3 using the experimental values for the ablation threshold.

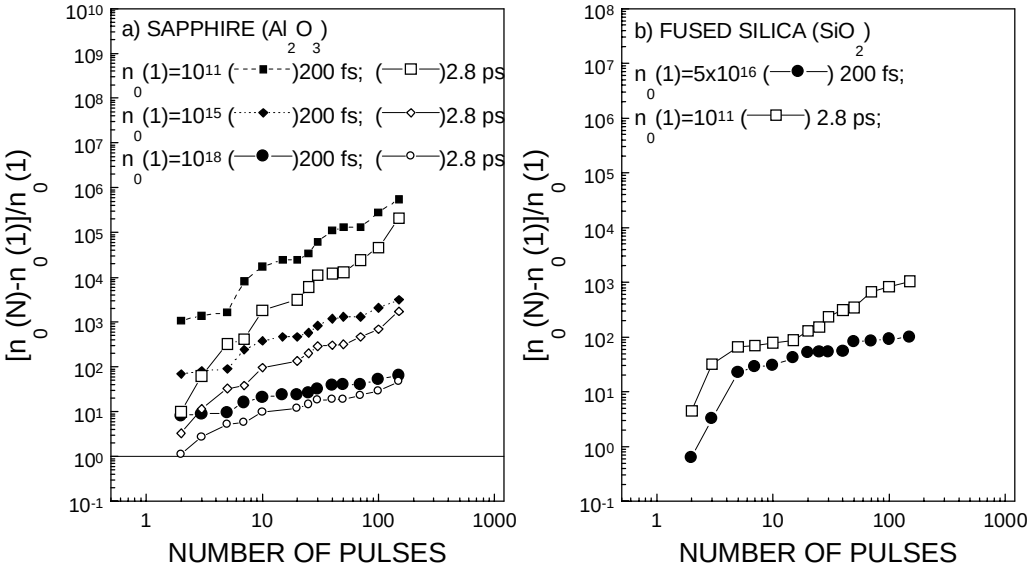

Fig. 3.2-5 Threshold defect accumulation process, based on the optical damage threshold model developed by Stuart et al. [SFH96] for 200 fs and 2.8 ps irradiation of sapphire and fused silica. The curves are calculated from Eq E 1.3-13 and Eq. E 3.2-3 using the experimental values for the ablation threshold.

Thus, one can write:

$$\frac{n_0(N)}{n_0(1)} = \exp\left[\left(\ln\left(\frac{n_0(1)}{n_{cr}}\right)\right)\left(\frac{F_{th}(N)}{F_{th}(1)}\right) - 1\right] \qquad \text{E 3.2-3}$$

$$n_0(1) \approx \int_{-\infty}^{\infty} P(I)dt$$

$$n_0(N) = \int_{-\infty}^{\infty} P(I)dt + \int_{-\infty}^{\infty} \sum_l \sigma_l D_l(N-1) I^l dt$$

where $D_l(N)$ is the laser induced defect density, N is the number of pulses per site, I is the laser intensity (similar to Eq. 1.3-10-1.3-15) and $\int P(I)dt$ and $\int \sigma_l D_l(N) I^l dt$ are the valence band and defects states' contributions respectively.

The result is presented in Fig. 3.2-4 and Fig. 3.2-5 for sapphire and fused silica for different seed electron densities (dependent on the initial active ionization centers' densities) and different pulse durations (we have to add that the depicted values are strongly dependent on the accuracy of the threshold determination). For fused silica typical multiphoton excitation at the threshold for N=1 ($n_0(1)=\int P(I_{th})$) are approx. 10^{16}-10^{17} cm^{-3} for 200 fs irradiation and approx. 10^{11}-10^{12} cm^{-3} for 2.8 ps irradiation, with a ratio $n(ps)/n(fs)$ of ~10^{-5}-10^{-6}. We note that the incubation effect (regarded as the electronic excitation originating from defect states) is stronger in the case of shorter pulses due to the efficient multiphoton excitation, and it is more efficient for initially pure samples.

We can write for the regime where defects are the main source for electrons:

$$\frac{n_{def}(ps)}{n_{def}(fs)} = \frac{\int_{-\infty}^{\infty} \sigma_D I_N^l(ps) D_N(ps)dt + \int_{-\infty}^{\infty} P(I_N(ps))dt}{\int_{-\infty}^{\infty} \sigma_D I_N^l(fs) D_N(fs)dt + \int_{-\infty}^{\infty} P(I_N(fs))dt} \approx \frac{\int_{-\infty}^{\infty} \sigma_D I_N^l(ps) D_N(ps)dt}{\int_{-\infty}^{\infty} \sigma_D I_N^l(fs) D_N(fs)dt} \qquad \text{E 3.2-4}$$

$$\frac{n_{def}(ps)}{n_{def}(fs)} \approx \frac{\left(\frac{F_N(ps)}{F_0(ps)}\right)^l D_N(ps) \int_{-\infty}^{\infty} \sigma_D I_0^l(ps)dt}{\left(\frac{F_N(fs)}{F_0(fs)}\right)^l D_N(fs) \int_{-\infty}^{\infty} \sigma_D I_0^l(fs)dt} \qquad \text{E 3.2-5}$$

For a temporally flat pulse the following expression can be derived:

$$\frac{n_{def}(ps)}{n_{def}(fs)} \approx \frac{\left(\frac{F_N(ps)}{F_0(ps)}\right)^l D_N(ps)}{\left(\frac{F_N(fs)}{F_0(fs)}\right)^l D_N(fs)} \left(\frac{F_0(ps)}{F_0(fs)}\right)^l \frac{\tau(ps)^{1-l}}{\tau(fs)} \qquad \text{E 3.2-6}$$

For $N \to \infty$ this becomes:

$$\frac{n_{def}(ps)}{n_{def}(fs)} \approx 20 \times 10^{-6 \div -8} \times \frac{D_{\infty}(ps)}{D_{\infty}(fs)} \qquad \text{E 3.2-7}$$

with n_{def}(2.8 ps)~10^{14} cm^{-3} and n_{def}(200 fs)~10^{18} cm^{-3} (see Fig. 3.2-5). This results in a rate: D_{∞}(2.8 ps)/D_{∞}(200 fs)~5÷500, depending on the excitation order *l*.

Thus, incubation manifests itself in two ways: a significant reduction in the ablation threshold and the crossover from gentle to strong ablation phases and it is related to defect accumulation upon multiple irradiation.

The ablation threshold has been measured as a function of the number of consecutive pulses, at low repetition rate (less than 1 Hz) so the accumulating heating effects can be neglected (although a stress load also associated with thermal effects may persist). A decrease in the ablation threshold by a factor of ~2 was observed after ~100 laser shots. The decrease is slightly stronger for irradiation with shorter laser pulses. The method for measuring the ablation threshold was given above. Fig. 3.2-6 indicates the threshold for ion removal from the irradiated sample at different pulse durations. Fig. 3.2-7 and Fig. 3.2-8 show the threshold dependence for both the gentle and the strong phase for both sapphire and fused silica. The appearance of the strong etch-phase is more difficult to distinguish for lower *N* and higher fluences and for higher pulse durations since the size of the defect affected region is counterbalanced by the higher ablation rates or annealing effect of the longer pulses respectively. Also, both phases are more distinct in an optical microscope in the case of sapphire as compared to fused silica or quartz samples due to different ablation rates and the appearance of the crater.

At the same time the pulse duration has a strong impact on the ablation threshold as illustrated in Fig. 3.2-6. Ps ablation has a higher threshold as compared to ablation with fs pulses. The difference can be explained on the basis of the MPI seeded avalanche model for optical damage presented in Chapter 1, i.e. the conditions to reach the critical electron density and the subsequent high absorption efficiency that will compensate the energy losses and will determine the occurrence of the damage.

The experimental threshold values derived in this work are with a factor of ~2 higher than those reported in [SFH96]. This is probably due to the fact that a number of 600 pulses per site have been used in [SFH96] for threshold determination, and, also a possible overestimation in the MPI and avalanche term in E 1.3-8 (see also Tables 1.3-1 and 1.3-2).

Quere and coworkers [QGM99] have shown that the breakdown threshold should not be defined as the achievement of a critical excitation density. The measured electron density at

the breakdown threshold decreases by one order of magnitude when the pulse duration is increased from 70 fs to 1.3 ps at 800 nm. This indicates the importance of phonon assisted free-electron heating as advocated by Jones et al. [JBC89]. The plasma critical density (i.e. strongly absorptive regime) should be regarded only as a theoretical indicator of macroscopic damage since the calculated threshold is not sensitive to this choice, varying with <20% when the electron density is one order of magnitude lower than the critical density [SFR95].

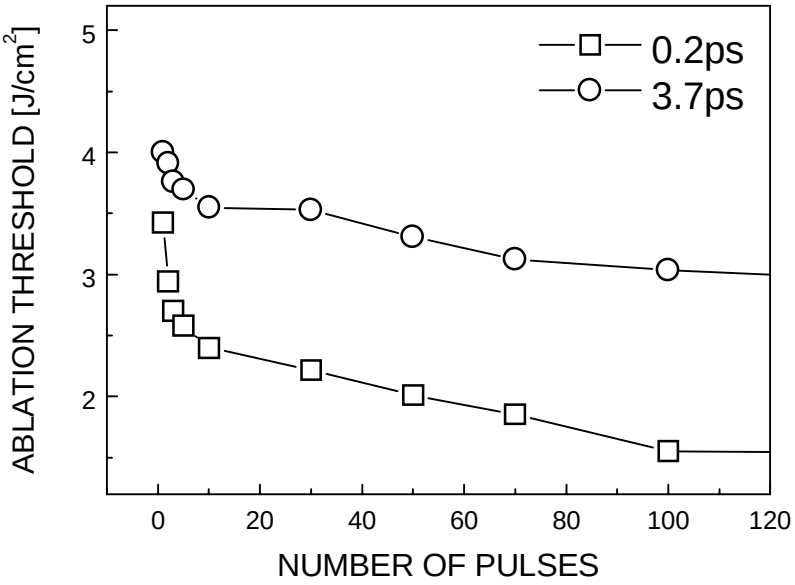

Fig. 3.2-6 Dependence of the ablation threshold for sapphire (indicated by the TOF signal) on the number of pulses for 0.2 ps and 3.7 ps. The *N*-dependence of the ablation threshold is regarded as a measure of the degree of incubation.

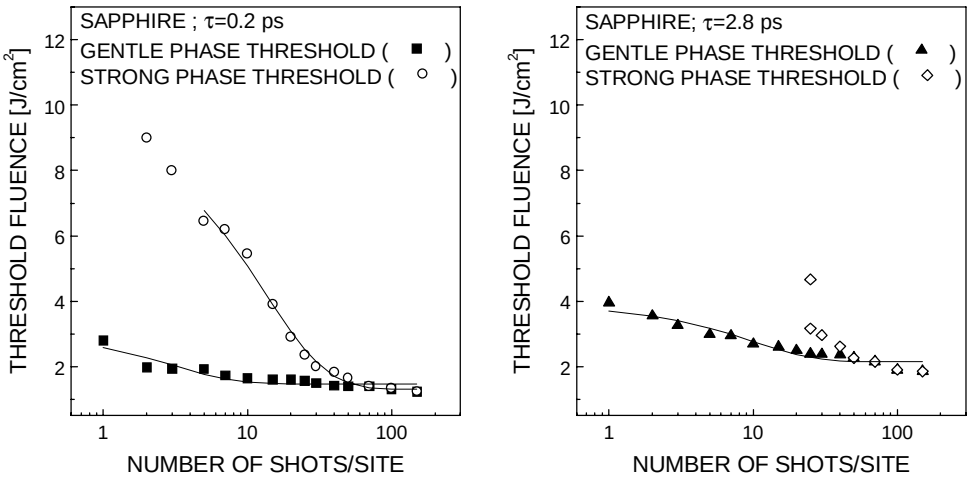

Fig. 3.2-7 Optical damage threshold values (obtained by the extrapolation of the damage dimensions to zero fluence, see text for details) for different ablation phases on sapphire at 0.2 and 2.8 ps irradiation. The fit curve is based on Eq. E 3.2-9.

Based on Eg. E-1.3-12 we can write, replacing the critical density value n_{cr} with the threshold value n_{th}:

$$\frac{F_{th}(ps)}{F_{th}(fs)} = 1 + \frac{\ln\left[\frac{n_{th}(ps)}{n_{th}(fs)}\frac{n_0(fs)}{n_0(ps)}\right]}{\ln\left[\frac{n_{th}(fs)}{n_0(fs)}\right]} \geq 1 \qquad \text{E 3.2-8}$$

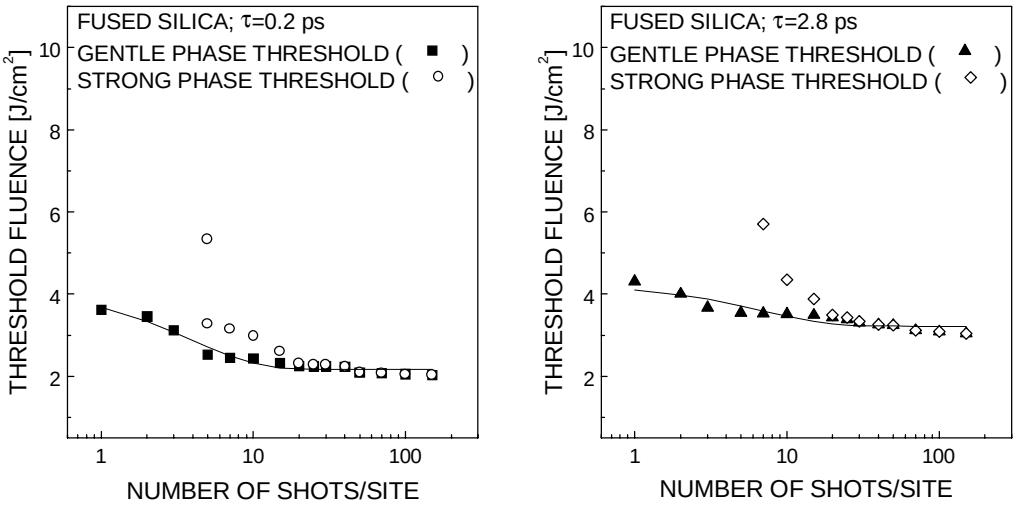

Fig. 3.2-8 Optical damage threshold values (obtained by the extrapolation of the damage dimensions to the zero fluence, see text for details) for different ablation phases on fused silica at 0.2 and 2.8 ps irradiation. The fit curve is based on Eq. E 3.2-9.

This is illustrated in Fig. 3.2-9, where the ratio between the 2.8 ps irradiation and 0.2 ps irradiation optical damage threshold is presented for sapphire and fused silica samples. The calculated ratio for 2.8 ps and 0.2 ps irradiation in the case of fused silica at 1053 nm (using the material constants from [SFH96]) is ~1.85. The estimations in the threshold fluences are based on numerical solving of Eq. E 1.3-8 and 1.3-14 and scaling the electron densities according to [QGM99].

The experimental ratio is smaller in the case of fused silica sample as compared to sapphire due lower electron density necessary to reach the threshold [QGM99] and efficient energy coupling to the lattice due to the fast trapping of the electrons. Indeed, according to [QGM99] $n_{th}(1.3\ ps)/\ n_{th}(70\ fs)$ is ~0.08 for fused silica and ~0.16 for sapphire at 800 nm laser irradiation, leading to the observed difference. The electron density necessary to reach the threshold becomes equal for sapphire and fused silica in the ps regime, leading to nearly equivalent thresholds. This is depicted in Fig. 3.2-10.

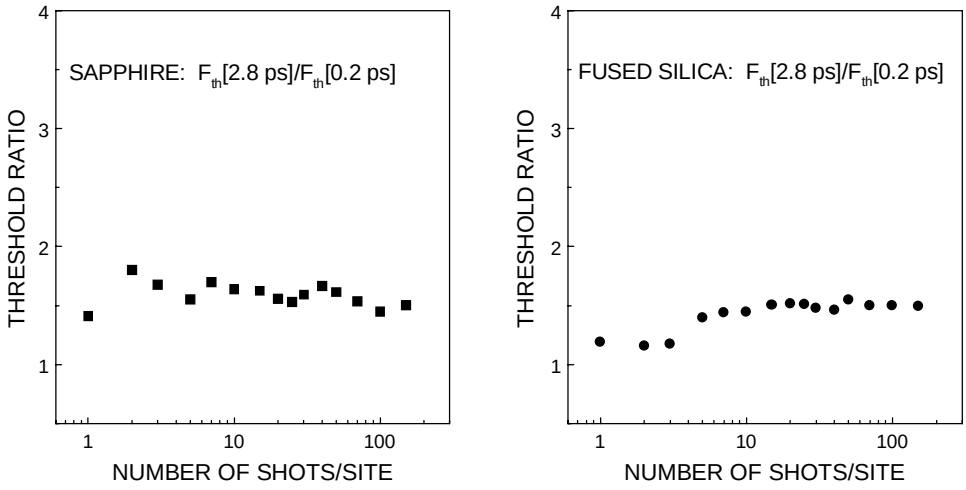

Fig. 3.2-9 Dependence of the optical damage threshold ratio between the 2.8 ps and 0.2 ps irradiation regimes for sapphire and fused silica on the number of pulses. The ratios are always above 1.

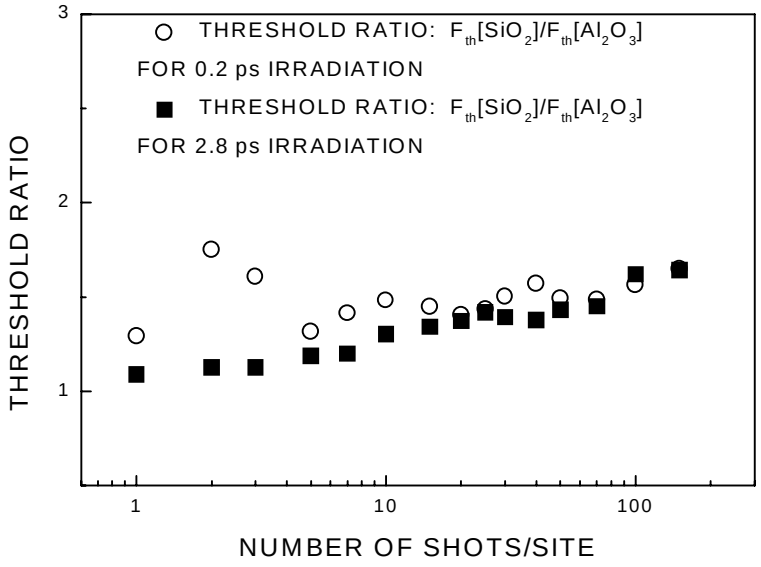

Fig. 3.2-10 Dependence of the ablation threshold ratio between fused silica and sapphire on the number of pulses per site for 0.2 ps and 2.8 ps.

The influence of the trapping mechanism on the threshold values at different pulse durations is depicted in Fig. 3.2-11. Considering electron trapping leads to an overestimation, since the rate equation similar to Eq E 1.3-14 does not take into account the fact that this energy is efficiently deposited into the lattice leading to damage. This shows that a criterion related only to the electron population is a rough approximation for the optical damage and

the channels for energy deposition into the lattice have to be considered in detail. The real values lie in the interval limited by the two extremes.

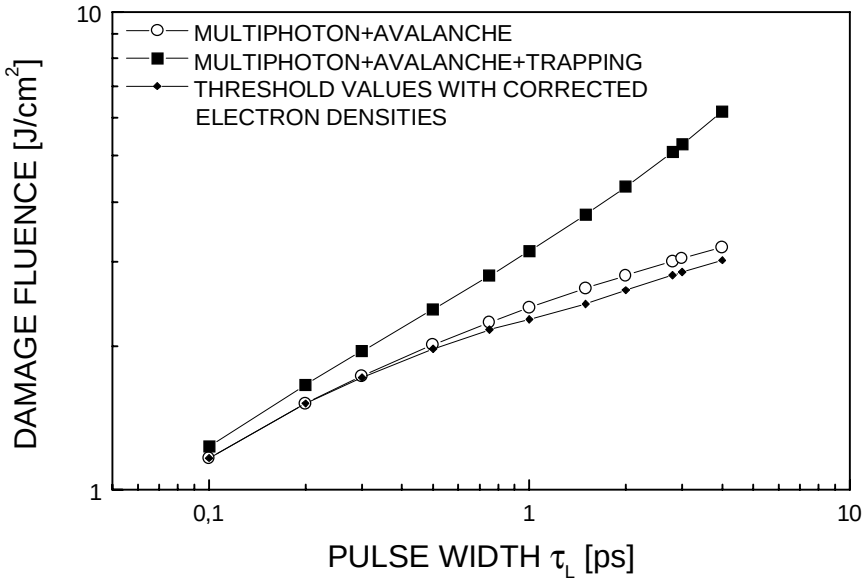

Fig. 3.2-11 Pulse width dependence of the threshold damage fluence for fused silica for different mechanisms considered in the rate equation Eq. E 1.3-14 (see text for details).

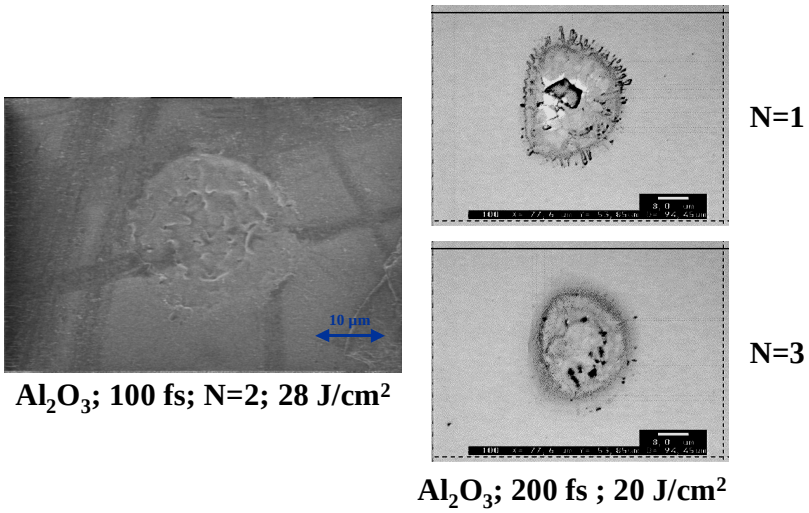

Fig. 3.2-12 Irradiated spot pictures showing the manifestation of the strong ablation phase in the case of sapphire at high energies: 20 J/cm^2 at 200 fs; 28 J/cm^2 at 100 fs.

The appearance of a strong phase at low number of shots in the case of high fluence irradiation is illustrated in Fig. 3.2-12 and is due to an efficient coupling of the energy to the lattice through enhanced thermal channels. Indeed, the strong ablation phase is the manifestation of a violent thermal mechanism which can be enhanced either by incubation (the coupling of the defects with the lattice will enhance the thermal energy deposition into the sample) or strong electron-phonon coupling and efficient heating.

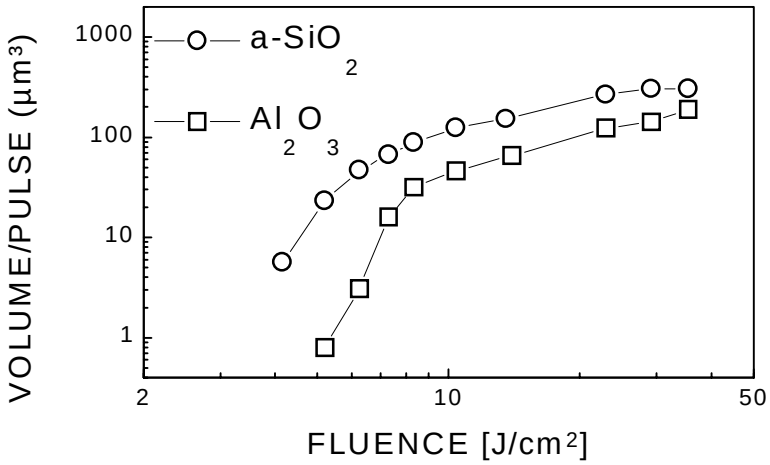

Fig. 3.2-13 The volume ablated per pulse (for the first laser pulse: N=1) versus the laser fluence. The augmentation in the ablation rate is a super-linear function, entering saturation at approx. 10 J/cm^2.

A very important effect of the laser fluence is the dramatic augmentation in the ablated volume per pulse for both fused silica and sapphire samples (Fig. 3.2-13). The augmentation is a super-linear function of the fluence entering saturation at about 10 J/cm^2 (this is also connected to the saturated reflectivity on a plasma boundary at supercritical electron densities, as extracted from the Fresnel formulas and the complex dielectric function [SFH96]). At this point thermal characteristics (droplets and melt traces) are observed in the optical microscope and SEM pictures of the ablated site (Fig. 3.2-12). The observed difference between fused silica and sapphire samples is due to a better thermal coupling of the energy to the lattice due to the faster carrier relaxation in the case of fused silica; 150 fs compared to 100 ps [PDG96].

Returning to multiple shot irradiation we can stress that, indeed, the defect accumulation process manifests itself in a reduction of the ablation threshold upon multiple irradiation. The accumulation process has an exponential behavior with the number of consecutive pulses, described by an incubation parameter in the following empirical equation.

According to Ashkenasi et al. [ASR2000] the surface damage threshold follows an exponential behavior at constant pulse durations.

$$F_{th}(N) = F_{th}(\infty) + [F_{th}(1) - F_{th}(\infty)]\exp(-k(N-1)) \qquad \text{E 3.2-9}$$

where $F_{th}(1)$ is the single shot threshold, $F_{th}(\infty)$-the asymptotic value for the threshold when $N \to \infty$ and k is an empirical parameter that characterizes the strength of the incubation leading to the reduction of the threshold. The equation is derived on the assumption that the increment in the defect concentration upon increasing number of pulses N is proportional to the product between the initial concentration and the increment in the number of pulses, and, the ablation

process is initiated at a certain defect density $D_{def}=D_{threshold}$ [MaG90]. This is the concentration of active ionization centers that provides sufficient electrons to achieve the critical density. Thus, it can be written:

$$\frac{dD(N)}{dN} = D(N)k_1 \qquad \text{E 3.2-10}$$

Assuming that k_1 depends only slightly on the employed fluence (it is related to the amount of excitation n_{cr}) and does not change for different N, we find:

$$D(N) = D_0 \exp(k_1 N) \text{ with } k_1 = k_1(F) \qquad \text{E 3.2-11}$$

When the defects themselves are able to provide enough electrons to reach the threshold, the electron multiplication process becomes almost insensitive to avalanche. The critical density is given therefore by (see also E 1.3-10-1.3-13):

$$n_{cr}(N) = n_{MPI}(N)\exp\left(\int_0^\infty \beta\, dt\right) \sim D(N-1)I^l \sim D(N-1)F_{th}^{\ l} \qquad \text{E 3.2-12}$$

Combining Eq. E 3.2-11 and E 3.2-12 (and neglecting the k_1 dependence on F) results:

$$F_{th} \sim \exp\left[-\frac{k_1}{l}(N-1)\right] \qquad \text{E 3.2-13}$$

The empirical observation can be also argued on the basis of the avalanche model developed by Stuart et al. [SFR95]. According to the rate equation E 1.3-8 and the simplifying conditions for Gaussian pulses E 1.3-10-1.3-13 one can write for different conditions of irradiation:

$$n(1) = n_0(1)\exp\left(\frac{\alpha}{2}F(1)\right) \qquad \text{with} \qquad n_0(1) = \int_{-\infty}^{\infty} P(I_1)dt \qquad \text{E 3.2-14}$$

$$n(N) = \left[n_0(N) + n_{def}(N)\right]\exp\left(\frac{\alpha}{2}F(N)\right) \qquad \text{E 3.2-15}$$

with $n_0(N) = \int_{-\infty}^{\infty} P(I_N)dt$ represents the valence band multiphoton term and $n_{def}(N) = \int_{-\infty}^{\infty} \sigma_l D_l (N-1) I^l dt$ is the additional MPI contribution from defects. For $N \to \infty$:

$$n(\infty) = \left[n_0(\infty) + n_{def}(\infty)\right]\exp\left(\frac{\alpha}{2}F(\infty)\right) \approx n_{def}(\infty)\exp\left(\frac{\alpha}{2}F(\infty)\right) \qquad \text{E 3.2-16}$$

At the threshold (i.e. when the electron population reaches approx. the critical density) one can write (*m* being the multiphoton order for the valence band excitation):

$$F_{th}(N)=\frac{2}{\alpha}\ln\frac{n_{cr}}{n_0(N)+n_{def}(N)}=\frac{2}{\alpha}\ln\frac{n_{cr}}{\int_{-\infty}^{\infty}P(I_N)dt+n_{def}(N)} \qquad \text{E 3.2-17}$$

where $P(I)\sim I^m$

$$F_{th}(N)=\frac{2}{\alpha}\ln\frac{n_{cr}}{\left(\frac{F(N)}{F(1)}\right)^m\int_{-\infty}^{\infty}P(I_1)dt+n_{def}(N)}$$

with $F=\int I(t)dt$ being the laser fluence.

Since the assumption of a constant rate k_1 growth is not very realistic, we can introduce a growth rate k_2 which depends also on the relative number of sites susceptible to be affected during the accumulation process at a certain fluence:

$$k_2(N,F(N))=k(F(N))\left(\frac{D_{def}(\infty)-D(N)}{D(N)}\right) \qquad \text{E 3.2-18}$$

$$\frac{dD(N)}{dN}=D(N)k_2=k\left(D_{def}(\infty)-D(N)\right) \qquad \text{E 3.2-19}$$

Since for any fluence *F(N)* leading to damage at different *N* the amount of laser induced excitation reaches a constant, critical value n_{cr} and *k* is essentially dependent on the amount of induced excitation, it can be considered that *k* is almost independent of fluence.

For multiple irradiation ($N>1$), the defect accumulation process can be described by:

$$D(N,F(N))=D(\infty,F(\infty))\left[1-C\exp(-kN)\right] \qquad \text{E 3.2-20}$$

$$n_{def}(N,F(N))=n_{def}(\infty,F(\infty))\left[1-C\exp\left[-k(N-1)\right]\right] \qquad \text{E 3.2-21}$$

where $D_{def}(\infty)$ represents the saturation defect density (with $n_{def}(\infty)$ being the electronic population developed from the defect states) and depends on the initial conditions of the sample (purity, etc.) and on the excitation conditions (laser fluence etc.) and *C* describes the initial conditions of the sample.

Thus, we can write:

$$F_{th}(N)=\frac{2}{\alpha}\ln\frac{n_{cr}}{\left(\frac{F(N)}{F(1)}\right)^l n_0(1)+n_{def}(\infty,F(\infty))\left[1-C\exp\left[-k(N-1)\right]\right]} \qquad \text{E 3.2-22}$$

$$F_{th}(N)=\frac{2}{\alpha}\ln\frac{n_{cr}}{n_0(1)}+\frac{2}{\alpha}\ln\frac{1}{\left(\frac{F(N)}{F(1)}\right)^{l}+\frac{n_{def}(\infty,F(\infty))}{n_0(1)}[1-C\exp[-k(N-1)]]} \quad \text{E 3.2-23}$$

Assuming that the defect electronic contribution is significant, Eq. E 3.2-23 can be reduced to:

$$F_{th}(N)\approx\frac{2}{\alpha}\ln\frac{n_{cr}}{n_0(1)}+\frac{2}{\alpha}\ln\frac{1}{\frac{n_{def}(\infty,F(\infty))}{n_0(1)}[1-C\exp[-k(N-1)]]} \quad \text{E 3.2-24}$$

Since $F_{th}(1)=\frac{2}{\alpha}\ln\frac{n_{cr}}{n_0(1)}$, it follows that: E 3.2-25

$$F_{th}(N)\approx F(1)+\frac{2}{\alpha}\ln\frac{n_0(1)}{n_{def}(\infty,F(\infty))[1-C\exp[-k(N-1)]]} \quad \text{E 3.2-26}$$

$$F_{th}(N)\approx F(1)-\frac{2}{\alpha}\ln\frac{n_{def}(\infty,F(\infty))[1-C\exp[-k(N-1)]]}{n_0(1)} \quad \text{E 3.2-27}$$

$$F_{th}(N)\approx F(1)-\frac{2}{\alpha}\ln\frac{n_{def}(\infty,F(\infty))}{n_0(1)}-\frac{2}{\alpha}\ln[1-C\exp[-k(N-1)]] \quad \text{E 3.2-28}$$

For $N\to\infty$ the above expression changes into:

$$F_{th}(\infty)\approx F(1)-\frac{2}{\alpha}\ln\frac{n_{def}(\infty,F(\infty))}{n_0(1)} \quad \text{E 3.2-29}$$

$$\frac{2}{\alpha}\ln\frac{n_{def}(\infty,F(\infty))}{n_0(1)}=F_{th}(1)-F_{th}(\infty) \quad \text{E 3.2-30}$$

From Eq. E 3.2-28 we receive the following:

$$F_{th}(N)\approx F(\infty)-\frac{2}{\alpha}\ln[1-C\exp[-k(N-1)]] \quad \text{E 3.2-31}$$

We can write thus (*ln*(x)~x-1):

$$F_{th}(N)\approx F(\infty)-\frac{2}{\alpha}\ln[1-C\exp[-k(N-1)]]\approx F(\infty)-\frac{2}{\alpha}[1-C\exp[-k(N-1)]-1] \quad \text{E 3.2-32}$$

This way:

$$F_{th}(N)\approx F(\infty)+\frac{2}{\alpha}C\exp[-k(N-1)] \quad \text{E 3.2-33}$$

similar to the situation described in [ASR2000].

This model has not taken into account the specific nature of the defects. The defects influence (either as isolated states in the band-gap, or as global a modification of the band-gap and related optical properties due to local stress load and subsequent modification of sample electronic structure) is basically regarded as a reservoir for electrons.

A relation similar to Eq. E 3.2-33 can describe the observed gentle-to-strong transition at constant fluence, but *k* will be dependent on the irradiation conditions since the employed fluences are above the threshold and, therefore, the amount of excitation is not limited to n_{cr} [SFH96], and may vary with *N*. Also, this argumentation holds for short pulses. For longer pulses where heating prevails (for example, due to free electron heating [JBC89]), the threshold may be associated with directly the achievement of the temperature necessary for phase transition rather than with a critical density (the electron density can be lower than the critical value [QGM99, NoV99]).

An alternative approach has been presented by Jones et al. [JBC89] for 70 ps pulses, based on build-up of local stress due to volume increase by the production of F-H pairs.

The situation is different for dielectrics as compared to metals or semiconductors where the incubation process is described by thermal stress-strain energy storage according to [SBW87, JBW88, PER89]:

$$NF_{th}(N,\tau_p) = F_{th}(1,\tau_p)N^S \qquad \text{E 3.2-34}$$

with $S<1$, characterizing the degree of incubation causing the surface fatigue following the stress load accumulated in the sample after repetitive irradiation.

3.3 Summary

This chapter discusses the different ablation phases at ultrashort, ps and sub-ps laser irradiation of dielectrics, and their distinct characteristics in terms of visual appearance, ablation rates and ionization efficiency. The gentle phase induced at low number of pulses per site is characterized by low ablation rates and high efficiency in ion production, while, at high number of shots per site, the strong phase is described by high ablation rates and characteristics of forceful removal of material of thermal nature. The crossover from the early gentle phase to the violent manifestation of the strong phase is related to incubation. The defect accumulation is also responsible for the reduction in the ablation threshold on multiple irradiation. The effects of the pulse duration and laser fluence are also investigated.